大阪公立大学 Osaka Metropolitan University 学術情報リポジトリ

Combined effects of molecular geometry and nanoconfinement on liquid flows through carbon nanotubes

メタデータ	言語: English 出版者: 公開日: 2020-01-31 キーワード (Ja): キーワード (En): 作成者: Suga, Kazuhiko, Mori, Yuki, Moritani, Rintaro, Kaneda, Masayuki メールアドレス: 所属:
URL	http://hdl.handle.net/10466/00016716

Combined effects of molecular geometry and nanoconfinement on liquid flows through carbon nanotubes

Kazuhiko Suga,* Yuki Mori, Rintaro Moritani, and Masayuki Kaneda
Department of Mechanical Engineering, Osaka Prefecture University, 1-1 Gakuen-cho, Naka-ku, Sakai, Osaka 599-8531, Japan

(Received 30 January 2018; revised manuscript received 12 April 2018; published 25 May 2018)

Molecular dynamics simulations are carried out to investigate the geometry effects of diatomic molecules on liquid flows in carbon nanotubes (CNTs). Oxygen molecules are considered as the fluid inside armchair (n,n) ($n = 6$–20) CNTs. The simulated fluid temperature and bulk pressure for the liquid state are $T = 133$ K and $\rho_b = 1346$ kg/m^3, respectively. In the agglomerated molecular cluster, nanoconfinement-induced structural changes are observed. As the CNT diameter decreases, it is confirmed that the flow rate significantly increases with irregular trends (discontinuity points in the profiles). From the discussion of the structure of the agglomerated fluid molecules, it is found that those trends are not simply caused by the structural changes. The main factor to induce the irregularity is confirmed to be the interlayer molecular movement affected by the combination of the molecular geometry and the arrangement of the multilayered structure.

DOI: 10.1103/PhysRevE.97.053109

I. INTRODUCTION

It is expected that carbon nanotubes (CNTs) [1] may change our daily lives through the innovation of materials applied to industrial devices because of their superior characteristics in strength and conductivity, etc. Due to the astonishingly very high flow rates through CNTs [2,3], CNTs can innovate the filters for water purification and solute separation [4–6]. Various other devices such as sensors by microelectromechanical-nanoelectromechanical system (MEMS-NEMS) [7–9] are also potential application fields of CNTs. Accordingly, many recent studies have focused on flows inside CNTs since it is necessary to understand the flow physics for bringing out better performance.

The measured flow rates of liquid water and hydrocarbons by Majumder *et al.* [2] were three to five orders of magnitude larger than those of the Hagen-Poiseuille flows for 7 nm diameter ($D = 7$ nm) tubes. For $D = 1.3$–2.0 nm tubes, the water flow rates by Holt *et al.* [3] were measured to be 560–8400 times as large as those of the Hagen-Poiseuille flows. Since the other measurements [10–12] also reported high flow rates of water and hydrocarbons for different ranges of the diameter, there is no doubt that large flow enhancements can be observed while some of the largest values may be unrealistic due to experimental difficulties or invalid data analysis. Moreover, there have been also many related molecular dynamics (MD) studies [13–31] reporting high flow rates. However, the reported levels of enhancement were scattered considerably. For the diameter range of $D = 1$–10 nm, Kannam *et al.* [30] summarized the literature and reported that the slip length, which is a measure of the flow rate, varied at least by two to three orders of magnitude.

As our previous study [32] discussed, it is considered that many different factors resulted in those scattering results. The simulation results depended on the molecular model used for water [33,34]. The ways to estimate the slip lengths and flow rate were also such factors. Some studies applied extrapolation of the velocity profiles assuming linear distributions near surfaces [28,35], others applied extrapolation of least-squares fitted velocity profiles [13] or calculation from the fitted parabolic function of the velocity profile [23] to obtain the slip lengths. To obtain volumetric flow rates, integrating velocity profiles using the bulk density, which was used in many studies, might have led to misleading conclusions. It is well known that the density near a wall tends to be nonuniformly layered [19,36] due to the attractive force by the wall molecules. With such layered density distribution, it is obvious that the parabolic Hagen-Poiseulle equation for the flow rate is no longer valid [37,38]. Hence, considering the axial density variation, our previous study [32] proposed a finite difference-based velocity fitting method to obtain consistent slip lengths.

The distribution profiles of the slip length and the flow rate sometimes showed kinks (discontinuous or singular points) [11,39]. To understand the flows in smaller pore diameters, Thomas and McGaughey [39] carried out an MD study and discussed the fluid structure and mechanisms of the flow rate enhancement of water flows through the armchair (6,6)-(12,12) CNTs. By their observation in the (9,9) CNT, water molecules formed a hexagonally shaped ring while pentagonal rings were formed in the (7,7) and (8,8) CNTs. Since only one single water molecule could be accommodated across the tube section in the (6,6) CNT, the water molecules formed a single-file molecular chain [14,15]. They noted that in such a condition water could not be a usual liquid [18] but a solidlike material. Since the bulklike liquid recovered at the (10,10) CNT, they observed that the flow enhancement ratio showed discontinuous transition between the (9,9) and (10,10) CNTs. They concluded that the confinement-induced structural change was the reason for the discontinuity. However, the experimental profile of the water flow rate by Qin *et al.* [11] showed a different trend from the (6,6) to (12,12) CNTs. Their measured transition occurred

*suga@me.osakafu-u.ac.jp

 ©2018 American Physical Society

between the (7,7) and (8,8) CNTs. For better understanding of such discontinuous transition in the flow rate, by simulating liquid argon flows, our previous study [32] discussed the relation between the flow rates and the cross sectional structure of the fluid molecules in the (6,6)–(160,160) CNTs. The study found that with the increase of the CNT diameter three-step transitional behaviors appeared. These were induced by the change of the structural arrangement of the fluid molecule cluster. The simulated trend of the flow rate qualitatively agreed with the result of Qin *et al.* [11] though the molecules were different. Since the sizes of the water and argon molecules are similar, it is considered that the confinement effects on water molecules were well simulated by the argon molecules.

These studies found that the cross-sectional structural arrangement of the fluid molecules had significant effects on the flow characteristics through CNTs. However, if the geometry of the fluid molecules is far from spherical, those findings may lose generality. Indeed, obviously hydrocarbon molecules are not spherical. Since the molecules of carbon dioxide, oxygen, and nitrogen have ellipsoidal or dumbbell-like shapes (though they are not that complicated), it is necessary to understand how such molecular geometry affects the confinement effects. Therefore, in this study, MD simulations of liquid flows of diatomic molecules (oxygen) inside CNTs are carried out.

II. MOLECULAR DYNAMICS SIMULATIONS

The present MD simulation code developed by our previous studies [32,40,41] applies the 6-12 Lennard-Jones (L-J) potential ϕ, which is defined as

$$\phi(r_{ij}) = 4\varepsilon\left[\left\{\left(\frac{\sigma}{r_{ij}}\right)^{12} - \left(\frac{\sigma}{r_{ij}}\right)^{6}\right\} - \left\{\left(\frac{\sigma}{r_c}\right)^{12} - \left(\frac{\sigma}{r_c}\right)^{6}\right\}\right], \tag{1}$$

where $r_{ij} = |\mathbf{r}_{ij}| = |\mathbf{r}_i - \mathbf{r}_j|$ is the intermolecular distance between molecules i and j, r_c is the cutoff radius, ε and σ are the well depth and the kinetic diameter of the molecules. In this system, the classical equation of motion of molecule i can be rewritten as

$$\frac{d^2\mathbf{r}_i^*}{dt^{*2}} = -\frac{\varepsilon\tau^2}{m\sigma^2}\sum_{j>i}\frac{\partial\phi^*}{\partial r_{ij}^*}\frac{\mathbf{r}_{ij}^*}{r_{ij}^*}, \tag{2}$$

where m, $r^* = r/\sigma, t^* = t/\tau (= t/\sqrt{m\sigma^2/\varepsilon})$, and $\phi^* = \phi/\varepsilon$ are the mass, the nondimensional distance, time, and energy, respectively. In calculations, to hold down the calculation effort of the interactions, the potential effects are truncated over with the cutoff distance defined as $r_c = 3\sigma$. For oxygen and carbon, the mass, the kinetic diameters, and the potential depths of $m_{O_2} = 5.32 \times 10^{-26}$ kg, $\sigma_O = 0.303$ nm, $\varepsilon_O = 0.667 \times 10^{-21}$ J, $m_C = 1.99 \times 10^{-26}$ kg, $\sigma_C = 0.34$ nm, and $\varepsilon_C = 0.455 \times 10^{-21}$ J are, respectively, applied and the Lorentz-Berthelot combining rules [42,43]:

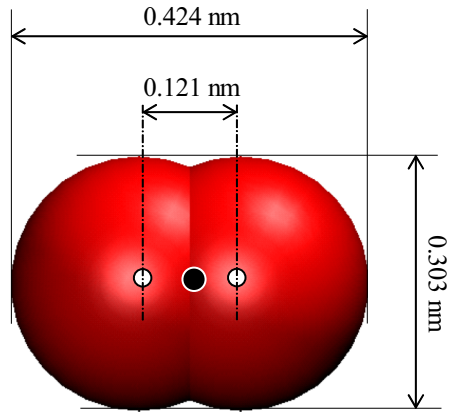

FIG. 1. Geometry of oxygen molecule; open and filled circles denote centres of mass of oxygen atoms and molecule, respectively.

$\sigma_{AB} = \frac{\sigma_A+\sigma_B}{2}, \varepsilon_{AB} = \sqrt{\varepsilon_A\varepsilon_B}$ are applied to the interaction between two dissimilar nonbonded atoms A-B. The oxygen molecules are represented by rigid two-site molecules with the bond length of 0.1207 nm. The geometry of the oxygen molecule used in this study is illustrated in Fig. 1. The molecular mass is divided equally into the sites (mass centers of the atoms). The sites are the points where L-J potential is applied. The rotational motion of an oxygen molecule is solved using the scheme of Fincham [44].

To the carbon-carbon bond whose length is set to 0.1421 nm, the Brenner potential [45] is applied and each carbon atom is tethered to the fixed space location by weak harmonic springs to avoid drifting of the CNT. The covalent bond energy is thus written as

$$E_b = \sum_i\sum_{j>i} f_c(r_{ij})[f_R(r_{ij}) - \bar{b}_{ij} f_A(r_{ij})], \tag{3}$$

where $f_c(r_{ij})$, $f_R(r_{ij})$, and $f_A(r_{ij})$ are the cutoff function, the repulsive, and the attractive energy terms of the potential, respectively. They are written as follows:

$$f_c(r_{ij}) = \begin{cases} 1, & r_{ij} \leqslant R^{(1)}, \\ \frac{1}{2}\left(1 + \cos\frac{r_{ij}-R^{(1)}}{R^{(2)}-R^{(1)}}\pi\right), & R^{(1)} < r_{ij} \leqslant R^{(2)}, \\ 0, & r_{ij} > R^{(2)}, \end{cases} \tag{4}$$

$$f_R(r_{ij}) = \frac{D_e}{S-1}\exp(-\lambda\sqrt{2S}(r_{ij} - R_e)), \tag{5}$$

$$f_A(r_{ij}) = \frac{D_e S}{S-1}\exp(-\lambda\sqrt{2S}(r_{ij} - R_e)), \tag{6}$$

where D_e, S, and R_e are determined by the physical properties of carbon. The bond order term is described as $\bar{b}_{ij} = \frac{b_{ij}+b_{ji}}{2}$. The function b_{ij} is written as $b_{ij} = [1 + \beta\zeta_{ij}]^{-\delta}$ where ζ_{ij} and

TABLE I. Parameters of the Brenner potential.

D_e (eV)	S	λ (Å^{-1})	R_e (Å)	$R^{(1)}$ (Å)	$R^{(2)}$ (Å)	β	δ	a	c	d	h
6.325	1.29	1.5	1.315	1.7	2.0	1.0	0.80469	0.011304	19	2.5	1.0

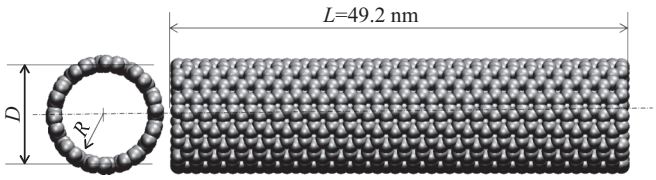

FIG. 2. Geometry of single-walled carbon nanotube.

$g_c(\theta)$ are, respectively, described as

$$\zeta_{ij} = \sum_{k\neq i,j} f_c(r_{ik}) g_c(\theta_{ijk}), \tag{7}$$

$$g_c(\theta_{ijk}) = a\left(1 + \frac{c^2}{d^2} - \frac{c^2}{d^2 + (h + \cos\theta_{ijk})^2}\right), \tag{8}$$

with θ_{ijk} the angle between bonds i-j and i-k. The parameters of the Brenner potential are tabulated in Table I.

The system temperature is kept constant by applying the Berendsen thermostat [46] to the CNT wall atoms. Figure 2 illustrates the geometry of the single-walled CNT. The armchair (6,6)–(20,20) CNTs with the axial length $L = 49.2$ nm are considered. The corresponding diameter ranges from $D =$ 0.81–2.71 nm. Table II lists the diameter D and the inner radius R of each CNT with the simulated numbers of wall and fluid molecules. The periodical inlet and outlet boundary conditions are applied. During the computations, to keep the oxygen in the liquid state, the temperature and the bulk fluid density are maintained at $T = 133$ K and $\rho_b = 1346$ kg/m^3. The corresponding mean molecular number density is $N^* =$ 25.3 nm^{-3}. The simulated condition is shown in the phase diagram of oxygen in Fig. 3. It clearly meets well the liquid condition. To drive flow in the axial direction, the external force of $f = 3.92 \times 10^{-15}$ N/molecule is applied to every fluid molecule. The computational time step is set to 0.54 fs and computations are performed for 43 ns to obtain statistical values after the designed temperature condition is satisfied.

III. RESULTS AND DISCUSSIONS

A. Enhancement of flow rate

Figure 4 shows snapshots of structures of liquid oxygen flows inside CNTs at $T = 133$ K and $\rho_b = 1346$ kg/m^3. Axial cross-sectional and side views are shown. Since the inner diameter of the (6,6) CNT is 0.47 nm, only a single oxygen molecule can well accommodate in the axial cross-sectional area. Due to the high pressure, a kind of zigzag-arranged single-file chain is formed in the axial direction. For the (7,7) and (8,8) CNTs, it is seen that a couple of molecules can accommodate in the cross-sectional area since the inner diameters are 0.61 and 0.75 nm. In the (9,9) CNT, a center core can be seen inside a ring

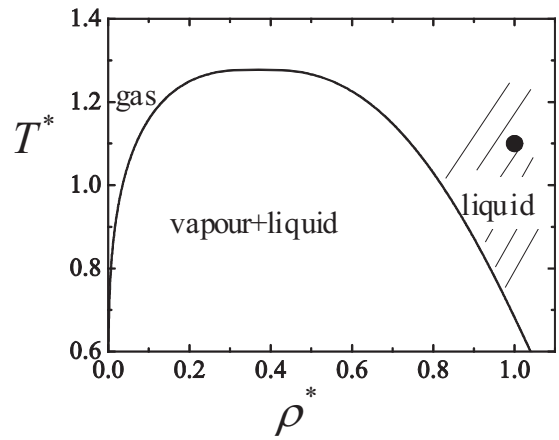

FIG. 3. Phase diagram of oxygen: filed circle denotes the simulated condition for the liquid state; $T^* = (k_B T)/\varepsilon$ and $\rho^* = \sigma^3 \rho_b / m$, k_B is the Boltzmann constant.

structure. As the diameter increases, the center core develops to the second ring followed by the emergence of another center core at the (14,14) CNT. Repeating these processes, the multilayered structure of agglomerated molecules develops as the chiral index increases.

Figure 5 shows the number density N and axial velocity u distributions across the CNTs. The number density distributions are normalized by the averaged number density N^*. Since each peak in the number density profile corresponds to a molecular layer, we can detect the structural change by examining the number density profiles. From the number density distributions, it is confirmed that the fluid molecules form a single-ring structure in the (7,7) and (8,8) CNTs while a center core appears at the (9,9) CNT and develops to another ring by the (13,13) CNT. These structural changes and the further development of the multilayered structure are consistent with those observed in Fig. 4.

As for the velocities, values are normalized by the friction-force-based velocity scale defined as $u_f = R^2 N^* f / \mu_\infty$, where μ_∞ is the bulk shear viscosity. Although the simulated velocity plots show scattering distributions, the fitting lines look very flat across the CNT diameters implying that fluid flows almost without friction. Note that the velocity fitting lines are produced by the method proposed by our previous study [32]. See Appendix for the details.

Using the simulated flow rate Q, the flow rate enhancement ε, which is the ratio between Q through the CNT and the nonslip Hagen-Poiseuille flow rate Q_{ns},

$$\varepsilon = Q/Q_{ns}, \tag{9}$$

TABLE II. Size of (n,n) carbon nanotubes and simulated numbers of molecules; D: diameter, R: inner radius.

chiral index: n	6	7	8	9	10	11	12	13	14	15	16	17	18	19	20
D (nm)	0.81	0.95	1.09	1.22	1.36	1.49	1.63	1.76	1.90	2.04	2.17	2.31	2.44	2.58	2.71
R (nm)	0.24	0.30	0.37	0.44	0.51	0.58	0.64	0.71	0.78	0.85	0.92	0.98	1.05	1.12	1.19
wall mol. no.	4800	5600	6400	7200	8000	8800	9600	10400	11200	12000	12800	13600	14400	15200	16000
fluid mol. no.	220	364	544	761	1013	1301	1626	1986	2382	2815	3284	3788	4329	4906	5519

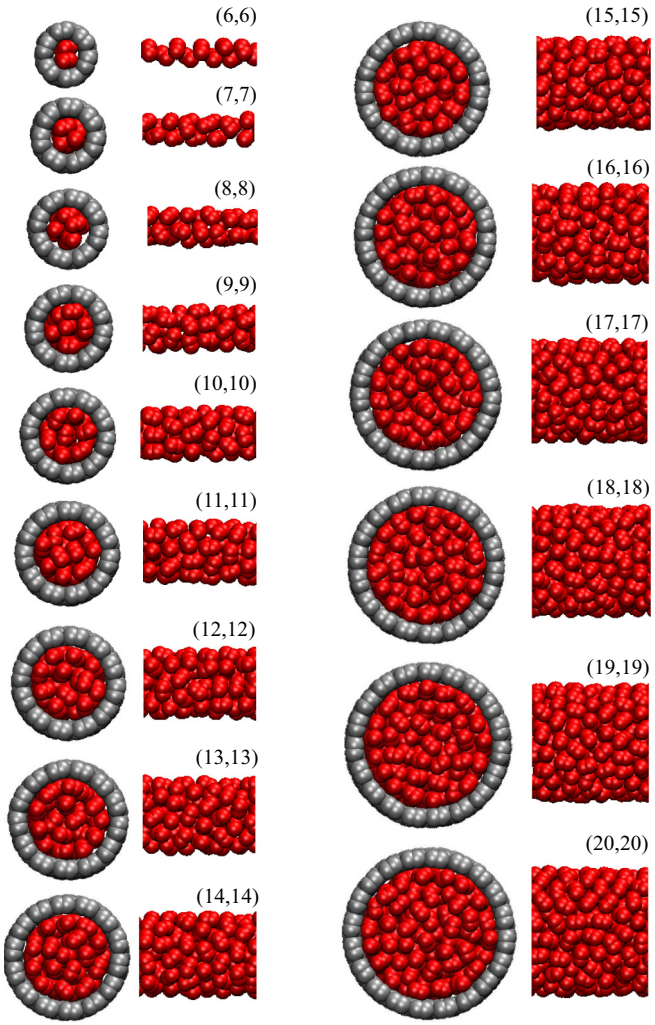

FIG. 4. Snapshots of structures of liquid oxygen flows inside CNTs at $T = 133$ K and $\rho_b = 1346$ kg/m^3; axial cross-sectional and side views. In the side views, carbon atoms are removed for clarity and the flow direction is from left to right.

is obtained as in Fig. 6. (Also see Appendix for the details of the calculation for ε.) The data of liquid argon flows [32] at $T = 121$ K and $\rho_b = 1344.3$ kg/m^3 are also compared. As seen in Fig. 6, like in the argon case, generally the flow rate enhancement becomes larger when the CNT diameter decreases. This trend is also confirmed in the velocity distribution levels shown in Fig. 5. Generally, the velocity level increases as the chiral index decreases. This is because the loss of the kinetic energy by the interaction between the fluid molecules is reduced in the narrower CNTs due to the fewer fluid molecules in the cross-sectional area.

In the distribution profiles of both oxygen and argon flows, several irregular trends can be observed. In the liquid argon case, such irregular phenomena were proved to be simply related to the changes of the cross-sectional structural arrangement of the fluid molecules [32]. When another center core appeared, ε started to drop rapidly. In the oxygen flows, as seen in Figs. 4 and 5(c), a center core appears at the (9,9) CNT and this leads to a slight drop of ε. However, a steeper drop occurs between the (7,7) and (8,8) CNTs while the single-ring structure is maintained as seen in Figs. 4 and 5(a), 5(b). As confirmed in Fig. 5(d), at the (10,10) CNT, the center core is maintained, but ε slightly recovers from the (9,9) CNT. At the (14,14) CNT, as seen in Fig. 5(f), another center core appears though ε recovers again from the (13,13) CNT. Hence, there seems to be no relation between these trends and the structural changes. This is inconsistent with the phenomena observed in the liquid argon flows.

B. Interlayer movement

To see what happens inside the CNTs more closely, Fig. 7 shows cross-sectional views of trajectories of sample molecules recorded in the time duration of 2.7 ns. The trajectories clearly indicate that the molecules move between the layers. Since such interlayer movement consumes further kinetic energy, the trajectory maps suggest that the flows with frequent such movement cannot maintain high flow rates. However, in the (6,6)–(8,8) CNTs, obvious interlayer movement is not observed implying that high flow rates are achieved in those CNTs. In the (10,10) CNT, although its cross-sectional structure has an outer layer with a center core as seen in Figs. 4 and 5(d), Fig. 7 suggests that movement between the center core and the outer layer is almost absent. Correspondingly, it is considered that compared with the (9,9) CNT case, even though the structural pattern does not change, the molecules in the (10,10) CNT are agglomerated tightly and flow faster. Such a tightly agglomerated cluster leads to highly efficient transport in the CNT that was called the "freight train" mechanism by Verweij *et al.* [18]. This is why ε recovers between the (9,9) and (10,10) CNTs.

To discuss the interlayer movement quantitatively, the interlayer momentum is defined as

$$M_{i-l} = \frac{(N_{i-l}/\Delta t)\delta r}{\bar{u}N^*}, \tag{10}$$

where $N_{i-l}/\Delta t$ is the counted number density of the molecules, which moves across the layers during the sampling time Δt and δr is the distance between layers. This is a measure of the interlayer movement. Figure 8 shows the distribution of the interlayer momentum M_{i-l} with the index of the layered structure. The indices of the layered structure of 0.5, 1, 1.5, 2, and 2.5 correspond to the single core, single layer (ring), single layer with a center core, double layer, and double layer with a center core structures, respectively. At the (6,6), (7,7), and (10,10) CNTs, M_{i-l} is almost zero while it generally increases as the CNT diameter increases. However, from the (9,9) to (10,10) and from (13,13) to (14,14) CNTs the interlayer momentum reduces. Since the smaller M_{i-l} means that the molecular cluster is more tightly agglomerated, the drops in the M_{i-l} distribution correspond to the recovering of ε observed in Fig. 6. Hence, the irregular patterns in the flow rate distribution are caused by the interlayer movement rather than the structural changes, which can be recognized by the change of the structural index in Fig. 8. Due to the cocoonlike nonspherical molecular shape, increasing layers does not necessarily mean loosening the tightness of the agglomeration. In the liquid argon flows, however, it is confirmed that the increase of the interlayer movement synchronizes the structural changes due to the spherical molecular shape.

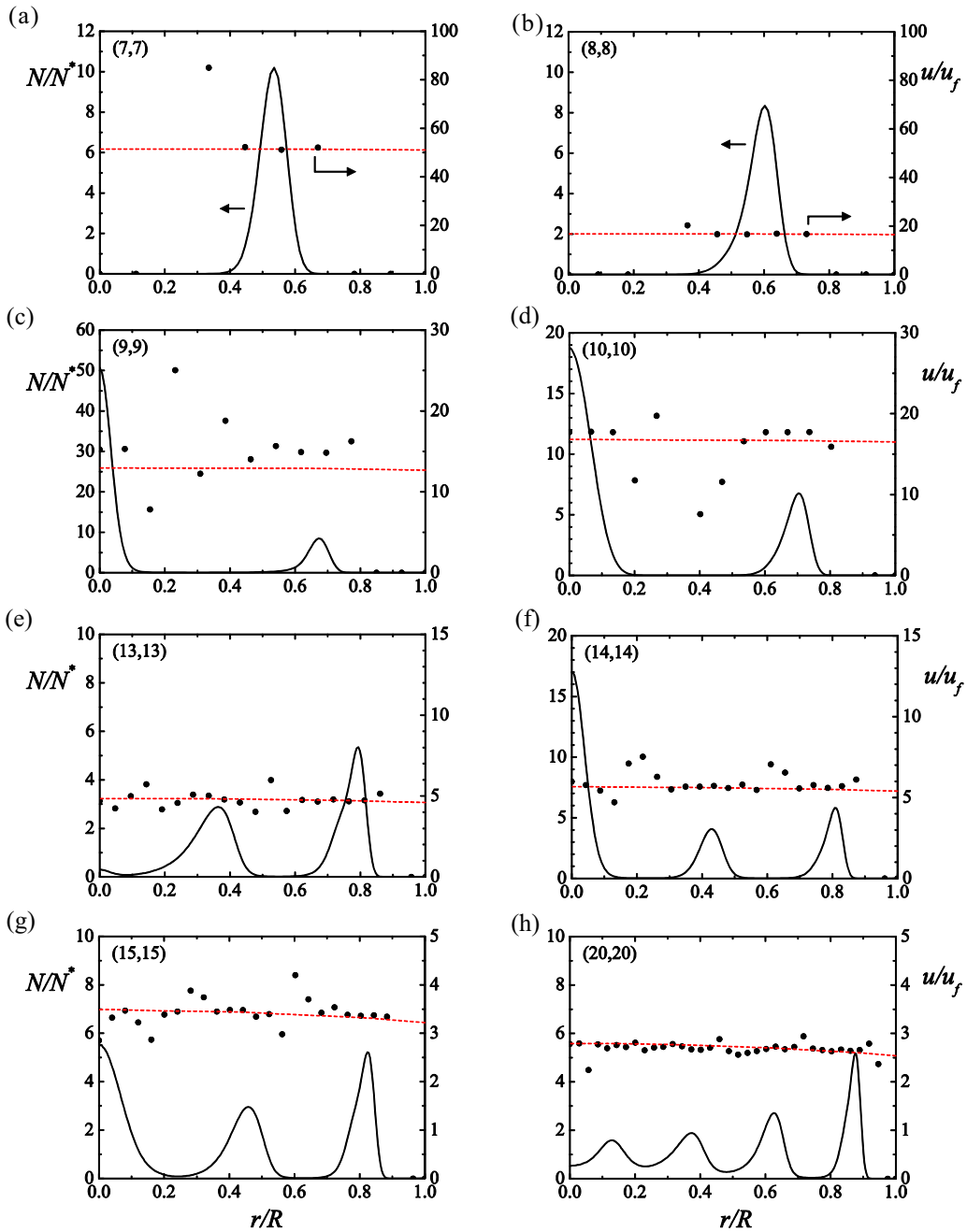

FIG. 5. Axial velocity u and number density N profiles of liquid oxygen flows inside CNTs at $T = 133$ K and $\rho_b = 1346$ kg/m^3; (a)–(h) correspond to the (7,7), (8,8), (9,9), (10,10), (13,13), (14,14), (15,15), and (20,20) CNTs; $u_f = R^2 N^* f/\mu_\infty$, μ_∞ and N^* are the bulk shear viscosity and the averaged number density, respectively; solid black lines and solid black circles denote number density and velocity distributions by the MD simulations, respectively; red broken lines are the velocity fitting lines by the method of Yasuoka *et al.* [32].

Although ε steeply drops between the (7,7) and (8,8) CNTs, there is no clue in the M_{i-l} distribution. Accordingly, to see the effects of the nonspherical molecular shape more in detail, the number density is recalculated by referring to the mass centers of oxygen atoms. Figure 9 compares this atomic mass-center-based number density with the (standard) molecular mass-center-based number density. At the (6,6) and (7,7) CNTs, both the atomic mass-center-based number density profiles indicate a simple spike distribution while at the (8,8) CNT it indicates that molecules distribute more widely having a plateau in its profile around $r/R \simeq 0.4$. This means that although the oxygen molecules maintain the single-ring structure, the molecules vibrate more significantly making the structure softer. Consequently, the flow rate drops between the (7,7) and (8,8) CNTs.

C. Orientational angles

Since diatomic molecules may possess orientational ordering, we further discuss on the effects of the orientation of the oxygen molecules on the flow rates inside the CNTs. Figure 10 illustrates orientational angles of an oxygen molecule in a CNT.

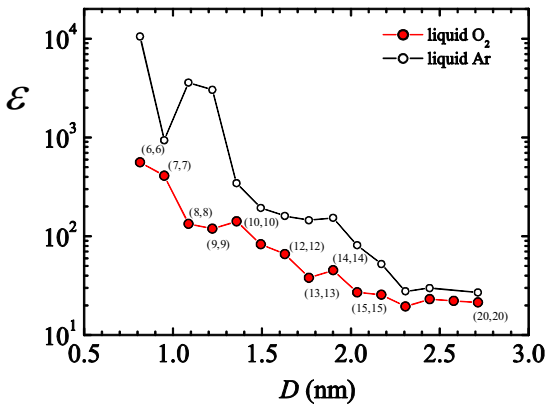

FIG. 6. Flow rate enhancement of liquid oxygen flows inside CNTs at $T = 133$ K and $\rho_b = 1346$ kg/m^3. Argon flow results of Yasuoka *et al.* [32] at $T = 121$ K and $\rho_b = 1344.3$ kg/m^3 are also plotted.

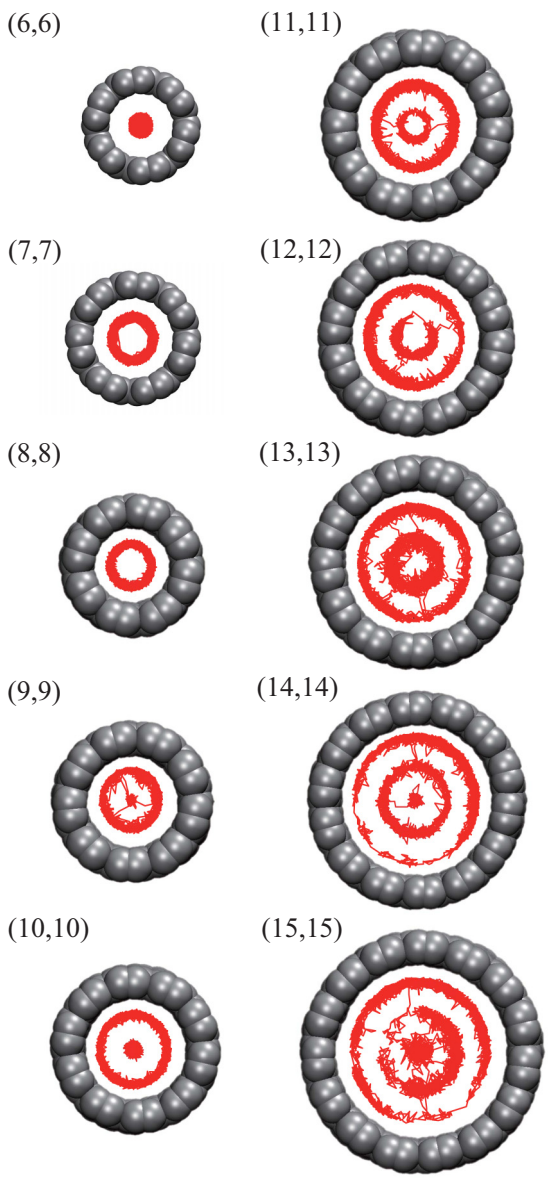

FIG. 7. Cross-sectional views of trajectories of liquid oxygen molecules.

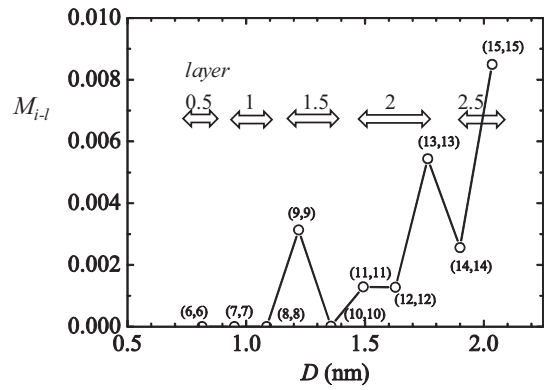

FIG. 8. Interlayer momentum of liquid oxygen flows and index of the layered structure; layer 0.5, 1, 1.5, 2, and 2.5 correspond to the single core, single layer (ring), single layer with a center core, double layer, and double layer with a center core structures, respectively.

Angles θ_r, θ_φ, and θ_z correspond to the angles between the molecular major axis vector $\overrightarrow{p_1 p_2}$ and r, r_p, z axes of the CNT, respectively. The CNT radial axis r passes through the site p_1 of the downstream atomic of the molecule while r_p corresponds to the one perpendicular to r and z is the axial direction of the CNT. Note that θ_r and θ_φ may have positive and negative signs though θ_z has a positive sign only.

Figures 11(a) and 11(b) compare the mean orientational angles $(\overline{\theta_r}, \overline{\theta_\varphi}, \overline{\theta_z})$ and their standard deviations $(\sigma_r, \sigma_\varphi, \sigma_z)$ calculated with all molecules through the simulations. Interestingly, as shown in Fig. 11(a), the axial mean angle is $\overline{\theta_z} \simeq 55^\circ$ for the CNTs larger than the (11,11) CNT. From Fig. 11(b), since its standard deviation is $\sigma_z \simeq 23^\circ$ for the CNTs larger than the (7,7) CNT, it is recognized that the axial angles of most molecules are in the range of $32^\circ \leqslant \theta_z \leqslant 78^\circ$ in the CNTs larger than the (11,11) case. Due to the symmetry, it is expected that the mean value of θ_φ becomes $\overline{\theta_\varphi} = 90^\circ$ irrespective of the CNT diameter D as seen in Fig. 11(a). The angle $\overline{\theta_r}$ is also tends to be close to 90° as D increases. Although $\overline{\theta_r}$ and $\overline{\theta_z}$ have oscillations depending on D, there seems to be no synchronization between them. However, the trend of $\overline{\theta_r}$ generally agrees with that of the flow rate enhancement. Indeed, the kinks at the (10,10) and (14,14) CNTs correspond to those in the flow rate enhancement shown in Fig. 6 though the levels of the oscillations are very slight [4° at the (10,10) and 2° at the (14,14) CNTs]. It is then difficult to consider that such a slight increase of the mean orientational angle affects the increase of the flow rate or vice versa.

When the molecules are tightly packed in the CNTs, it may be considered that the tightness affects the standard deviations of the orientational angles. If the tightness and the standard deviation of the orientational angle have a correlation, it can be considered that when the interlayer momentum becomes large the standard deviation is also large. Indeed, for the (13,13) and (15,15) CNTs, σ_r becomes larger than both neighbors corresponding well to the spikes of the interlayer momentum shown in Fig. 8. However, σ_z and σ_φ do not show such a trend. [Rather than increasing, σ_φ slightly decreases at the (13,13) and (15,15) CNTs.] Furthermore, none of the standard deviations corresponds to the spike of the interlayer momentum at the (9,9) CNT. Accordingly, since the motion of liquid

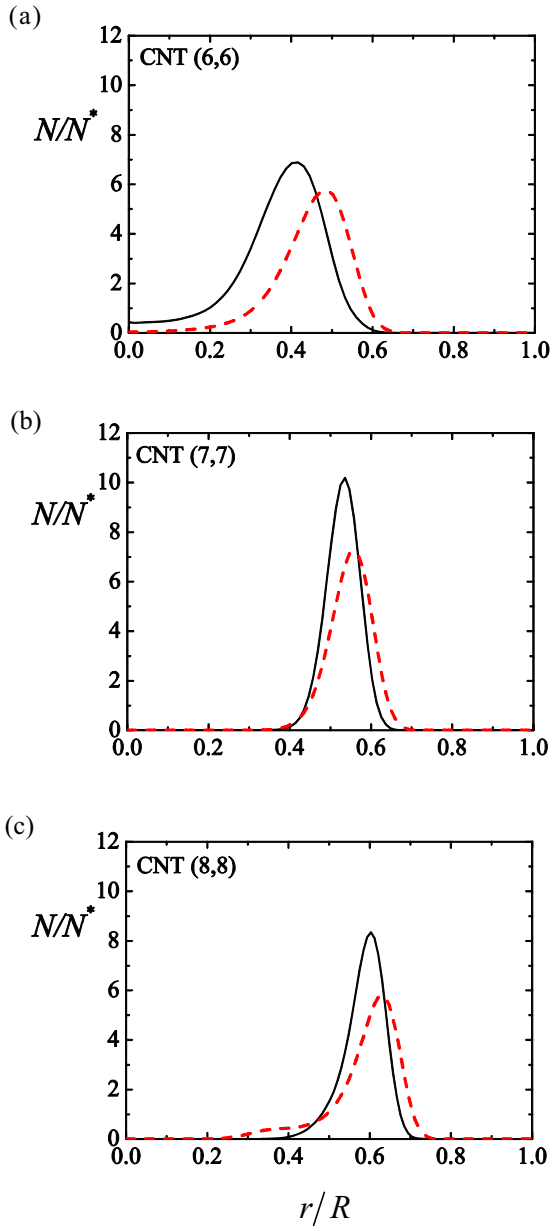

FIG. 9. Comparison of number density profiles of liquid oxygen flows inside CNTs at $T = 133$ K and $\rho_b = 1346$ kg/m^3; (a)–(c) correspond to the (6,6), (7,7), and (8,8) CNTs; solid black lines and red broken lines indicate the molecular mass-center number density and atomic mass-center-based number density profiles, respectively.

molecules has a large degree of freedom, even for the diatomic molecules, systematic effects of orientational ordering of the fluid molecules on the flow rates are hardly observed.

IV. CONCLUDING SUMMARY

To investigate the geometry effects of diatomic fluid molecules on the nanoconfinement to the liquid flows in carbon nanotubes (CNTs), molecular dynamics simulations are carried out. Oxygen flows through armchair (n,n) $(n = 6$–$20)$ CNTs are considered. The fluid temperature and bulk pressure are $T = 133$ K and $\rho_b = 1346$ kg/m^3, respectively. In the

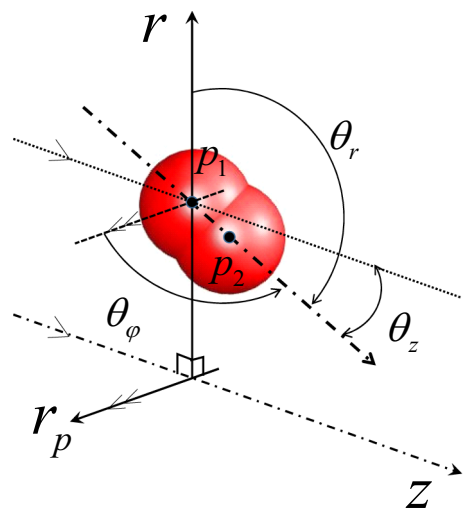

FIG. 10. Definition of orientational angles: $\theta_r, \theta_\varphi, \theta_z$; r and z axes are the cylindrical coordinate axes of a CNT, sites p_1, p_2 are the atomic mass centers of an oxygen molecule.

liquid flow, the oxygen molecules form a layered structure and increase the layer number as the CNT diameter becomes large, like liquid argon and water flows. Also like those fluids, it is

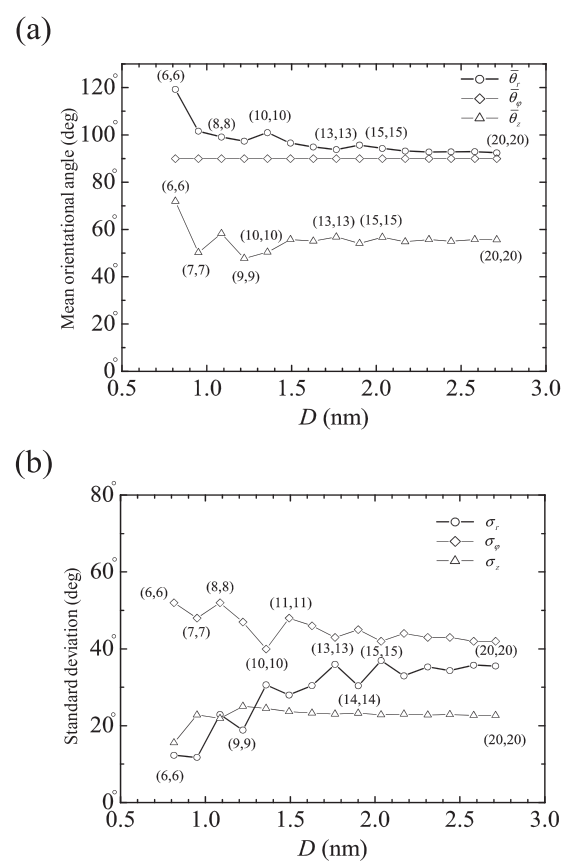

FIG. 11. Orientational angles of oxygen molecules inside CNTs at $T = 133$ K and $\rho_b = 1346$ kg/m^3; (a) mean orientational angles, (b) standard deviation of the orientational angles.

observed that the flow rate significantly increases with irregular discontinuity points as the chiral index decreases. However, unlike in those fluids, it is confirmed that the structural changes are not responsible for the irregularity by the observation of the agglomerated structure of the oxygen molecules and the number density distribution. From the discussion of the molecular trajectory and the movement between the structural layers, it is concluded that the main factor to induce the irregularity is such interlayer movement. When the interlayer movement becomes less frequent, the tightness of the agglomerated molecular cluster increases leading to a higher flow rate. In the fluids of spherical molecules, the interlayer movement is enhanced as the increase of the layers (structural change). However, for the diatomic molecules, due to the dumbbell- or cocoon-like shape, the interlayer movement of the agglomeration does not simply depend on the layer number nor orientational ordering of the fluid molecules. It results from the complex combination of the molecular geometry and the arrangement of the multilayered structure of the fluid molecules.

APPENDIX

To fit the relatively scattered velocity plot points of the MD simulations, solving the transport equation with variable density is carried out. The fully developed steady-state momentum equation in a CNT is written as

$$0 = \frac{1}{r}\frac{\partial}{\partial r}\left(r\mu\frac{\partial u(r)}{\partial r}\right) + F_z(r), \tag{A1}$$

where r, μ, u, and F_z are the radial coordinate, shear viscosity, axial (z) velocity, and axial body force acting on the unit fluid volume, respectively. For the external force field, $F_z(r) = fN(r)$ where N, f are the number density of fluid molecules and the external force acting on each fluid molecule. By the normalization: $\tilde{r} = r/R, \tilde{\mu} = \mu/\mu_\infty$ and $\tilde{u} = u/u_f$, where $u_f = R^2\overline{F_z}/\mu_\infty, \overline{F_z} = N^* f$, and R, μ_∞, N^* are the CNT inner radius, the bulk shear viscosity of the fluid, and the averaged number density of the fluid molecules, respectively, equation (A1) is rewritten as

$$\frac{\partial}{\partial \tilde{r}}\left(\tilde{r}\tilde{\mu}\frac{\partial \tilde{u}}{\partial \tilde{r}}\right) = -\tilde{r}N/N^*. \tag{A2}$$

Here, an overlined variable is a volume or sectionally averaged variable. Equation (A2) is numerically integrated by the finite difference method (FDM) using the number density distribution obtained by the MD simulation. As for the shear viscosity, we simply apply $\tilde{\mu} = 1$ ($\mu = \mu_\infty$) to solve equation (A2). Iterative calculations of the discretized equation are carried out with the boundary conditions, $\partial u/\partial r = 0$ at the axis and $u = u_R$ on the surface. Since the slip velocity u_R is unknown beforehand, first the nonslip wall condition is applied to obtain the velocity profile of $u^{**}(= \tilde{u} - \tilde{u}_R)$. Then, the slip velocity $\tilde{u}_R$ is calculated using the mass flow rate $\dot{m}$ obtained by counting the fluid molecules passing through a sampling section during the MD simulation. Since the mass flow rate is

$$\dot{m} = 2\pi\int_0^R \rho u r dr = 2\pi R^2 u_f \int_0^1 \rho(u^{**} + \tilde{u}_R)\tilde{r}d\tilde{r}, \tag{A3}$$

the slip velocity $\tilde{u}_R$ is calculated as

$$\tilde{u}_R = \frac{Q - 2\int_0^1 (N/N^*)u^{**}\tilde{r}d\tilde{r}}{2\int_0^1 (N/N^*)\tilde{r}d\tilde{r}}, \tag{A4}$$

where the normalized volumetric flow rate is $Q(= \frac{\dot{m}}{\bar{\rho}\pi R^2 u_f})$. This slip velocity is essentially a half of the slip length $\tilde{L}_s$ since the total force acting to the liquid molecules should balance with the total friction:

$$-\mu\left.\frac{du}{dr}\right|_{r=R} \times 2\pi RL = fN^*\pi R^2 L, \tag{A5}$$

and $\frac{d\tilde{u}}{d\tilde{r}}|_{\tilde{r}=1} = -\frac{1}{2}$. From these relations,

$$\tilde{L}_s = L_s/R = -\tilde{u}_R/\left.\frac{d\tilde{u}}{d\tilde{r}}\right|_{\tilde{r}=1} = 2\tilde{u}_R. \tag{A6}$$

It is clear that the flow rate does not depend on the velocity profile but it depends on the external force acting on the flow system. Since the normalized flow rate becomes $Q_{ns} = 1/8$ for the nonslip isodensity flow (Hagen-Poiseuille flow), the flow rate enhancement is obtained as

$$\varepsilon = Q/Q_{ns} = 8Q. \tag{A7}$$

[1] S. Iijima, Nature (London) **354**, 56 (1991).
[2] M. Majumder, N. Chopra, R. Andrews, and B. J. Hinds, Nature (London) **438**, 44 (2005).
[3] J. K. Holt, H. G. Park, Y. Wang, M. Stadermann, A. B. Artyukhin, C. P. Grigoropoulos, A. Noy, and O. Bakajin, Science **312**, 1034 (2006).
[4] B. J. Hinds, N. Chopra, T. Rantell, R. Andrew, V. Gavalas, and L. G. Bachas, Science **303**, 62 (2004).
[5] Y. Murakami, S. Chiashi, Y. Miyauchi, M. Hu, M. Ogura, T. Okubo, and S. Maruyama, Chem. Phys. Lett. **385**, 298 (2004).
[6] D. S. Sholl and J. K. Johnson, Science **312**, 1003 (2006).
[7] D. R. Miller, S. A. Akbar, and P. A. Morris, Sens. Actuators, B **204**, 250 (2014).
[8] T. Plecenik, M. Moško, A. Haidry, P. Ďurina, M. Truchlý, B. Grančič, M. Gregor, T. Roch, L. Satrapinskyy, A. Mošková, M. Mikula, P. Kúš, and A. Plecenik, Sens. Actuators, B **207, Part A**, 351 (2015).
[9] M. Vallikivi and A. J. Smits, J. Microelectromech. Sys. **23**, 899 (2014).
[10] F. Du, L. Qu, Z. X. L. Feng, and L. Dai, Langmuir **27**, 8437 (2011).
[11] X. Qin, Q. Yuan, Y. Zhao, S. Xie, and Z. Liu, Nano Lett. **11**, 2173 (2011).
[12] M. Whitby, L. Cagnon, M. Thanou, and N. Quirke, Nano Lett. **8**, 2632 (2008).
[13] V. P. Sokhan, D. Nicholson, and N. Quirke, J. Chem. Phys. **115**, 3878 (2001).

[14] G. Hummer, J. C. Rasaiah, and J. P. Noworyta, Nature (London) **414**, 188 (2001).
[15] A. Kalra, S. Garde, and G. Hummer, Proc. Natl. Acad. Sci. USA **100**, 10175 (2003).
[16] E. M. Kotsalis, J. H. Walther, and P. Koumoutsakos, Int. J. Multiphase Flow **30**, 995 (2004).
[17] I. Hanasaki and A. Nakatani, J. Chem. Phys. **124**, 144708 (2006).
[18] H. Verweij, M. C. Schillo, and J. Li, Small **3**, 1996 (2007).
[19] S. Joseph and N. R. Aluru, Nano Lett. **8**, 452 (2008).
[20] X. Chen, G. Cao, A. Han, V. K. Punyamurtula, L. Liu, P. J. Culligan, T. Kim, and Y. Qiao, Nano Lett. **8**, 2988 (2008).
[21] J. A. Thomas and A. J. H. McGaughey, J. Chem. Phys. **128**, 084715 (2008).
[22] J. A. Thomas and A. J. H. McGaughey, Nano Lett. **8**, 2788 (2008).
[23] J. A. Thomas, A. J. H. McGaughey, and O. Kuter-Arnebeck, Int. J. Therm. Sci. **49**, 281 (2010).
[24] K. Falk, F. Sedlmeier, L. Joly, R. R. Netz, and L. Bocquet, Nano Lett. **10**, 4067 (2010).
[25] J. S. Babu and S. P. Sathian, J. Chem. Phys. **134**, 194509 (2011).
[26] J. S. Hansen, B. D. Todd, and P. J. Daivis, Phys. Rev. E **84**, 016313 (2011).
[27] T. Mutat, J. Adler, and M. Sheintuch, J. Chem. Phys. **136**, 234902 (2012).
[28] K. Falk, F. Sedlmeier, L. Joly, R. R. Netz, and L. Bocquet, Langmuir **28**, 14261 (2012).
[29] S. K. Kannam, B. D. Todd, J. S. Hansen, and P. J. Daivis, J. Chem. Phys. **136**, 244704 (2012).
[30] S. K. Kannam, B. D. Todd, J. S. Hansen, and P. J. Daivis, J. Chem. Phys. **138**, 094701 (2013).
[31] E. Chiavazzo, M. Fasano, P. Asinari, and P. Decuzzi, Nature Commun. **5**, 3565 (2014).
[32] H. Yasuoka, R. Takahama, M. Kaneda, and K. Suga, Phys. Rev. E **92**, 063001 (2015).
[33] A. Alexiadis and S. Kassinos, Molecul. Simul. **34**, 671 (2008).
[34] L. Liu and G. N. Patey, J. Chem. Phys. **141**, 18C518 (2014).
[35] S. C. Kassinos, J. H. Walther, E. M. Kotsalis, and P. Koumoutsakos, in *Multiscale Modelling and Simulation*, edited by S. Attinger and P. Koumoutsakos (Springer Verlag, New York, 2004), pp. 215–226.
[36] A. Alexiadis and S. Kassinos, Chem. Eng. Sci. **63**, 2047 (2008).
[37] K. P. Travis and D. J. Evans, Phys. Rev. E **55**, 1566 (1997).
[38] K. P. Travis and K. E. Gubbins, J. Chem. Phys. **112**, 1984 (2000).
[39] J. A. Thomas and A. J. H. McGaughey, Phys. Rev. Lett. **102**, 184502 (2009).
[40] H. Yasuoka, T. Imae, M. Kaneda, and K. Suga, J. Therm. Sci. Tech. **10**, 15 00453 (2015).
[41] H. Yasuoka, M. Kaneda, and K. Suga, J. Stat. Phys. **165**, 907 (2016).
[42] D. C. R. Berthelot, Hebd. Seanc. Acad. Sci. (Paris) **126**, 1703 (1898).
[43] H. A. Lorentz, Ann. Phys. (N.Y.) **248**, 127 (1881).
[44] D. Fincham, CCP5, Info. Quart. **2**, 6 (1981).
[45] D. W. Brenner, Phys. Rev. B **42**, 9458 (1990).
[46] H. J. C. Berendsen, J. P. M. Postma, W. F. van Gunsteren, A. DiNola, and J. R. Haak, J. Chem. Phys. **81**, 3684 (1984).